Nanoscale Advances

ROYAL SOCIETY OF CHEMISTRY

PAPER

View Article Online
View Journal | View Issue

Cite this: *Nanoscale Adv.*, 2025, **7**, 7196

Engineered riboflavin–cerium oxide nanoparticles for enhanced phototoxicity toward triple-negative breast cancer cells

Anongnat Wongpan, [a] Sopon Nuchpun,[a] Napasorn Tana-atsawapon,[a] Patraporn Luksirikul, [bc] Sarisa Suriyarak, [d] Jintana Artsanthia[e] and Kanlaya Prapainop Katewongsa *[a]

Cerium oxide nanoparticles (CeO_2 NPs) are redox-active nanomaterials with promising applications in biomedical engineering. In this study, CeO_2 NPs are functionalized with riboflavin to enhance cellular uptake and introduce photoresponsive properties. *In vitro* studies demonstrate that the resulting riboflavin-modified CeO_2 (Rf–CeO_2) NPs exhibit low toxicity under dark conditions but exert significantly enhanced cytotoxicity against triple-negative breast cancer (TNBC) MDA-MB-231 cells upon ultraviolet (UV) irradiation. This light-triggered cytotoxic effect is attributed to the photoactive nature of riboflavin, which alters reactive oxygen species (ROS) generation upon UV exposure. Our findings highlight the potential of Rf–CeO_2 NPs as a selectively light-activated nanoplatform for targeted cancer therapy that integrates redox functionality and photoactivity into a single engineered nanomaterial, particularly for TNBC and other aggressive cancer subtypes.

Received 5th June 2025
Accepted 9th September 2025

DOI: 10.1039/d5na00555h

rsc.li/nanoscale-advances

1. Introduction

Breast cancer is a major global health burden. It is a highly heterogeneous malignancy that presents with multiple subtypes, each with distinct molecular and epidemiological characteristics.[1] Triple-negative breast cancer (TNBC), a subtype defined by the absence of the estrogen receptor, progesterone receptor, and human epidermal growth factor receptor 2 (HER2), accounts for approximately 10–20% of all breast cancers and is associated with poor prognosis, high recurrence rates, and limited therapeutic approaches. Conventional treatments, such as surgery, radiation, and chemotherapy, are largely ineffective against TNBC.[2–5] These challenges signify the need for innovative therapeutic approaches that can selectively target cancer cells while minimizing damage to healthy tissues.[6]

Nanotechnology offers new platforms for administering cancer treatment, such as drug delivery, molecular targeting, and therapeutic activation.[7] Among various nanomaterials, cerium oxide nanoparticles (CeO_2 NPs), or nanoceria, have emerged as promising nanotherapeutic agents because of their distinctive redox-active properties, which facilitate potent antioxidant activity and potentially confer anticancer effects.[8–10] Cerium, a rare-earth element and the second within the lanthanide series, is distinguished by its unique ability to reversibly transition between Ce^{3+} and Ce^{4+} oxidation states, which coexist on the NP surface through oxygen vacancy-mediated redox cycling.[11] These redox properties enable nanoceria to mimic the catalytic functions of key antioxidant enzymes, such as catalase (CAT) and superoxide dismutase (SOD), thereby facilitating the scavenging of reactive oxygen species (ROS) and attenuating oxidative stress in biological systems.[12,13] In cancer therapy, this redox modulation can fulfil the dual roles of protecting normal cells from oxidative stress while promoting oxidative damage in tumor cells, thereby inducing apoptosis or increased treatment sensitivity.[14] In TNBC, redox imbalances and elevated basal ROS levels are often exploited, and further induction of ROS can trigger cancer cell death, overcome therapeutic resistance, and enhance chemotherapeutic efficacy while sparing normal cells.[15,16]

Nanoceria has stood out as a promising therapeutic agent in breast cancer because of its ability to modulate intracellular ROS, which is crucial in tumor progression, therapeutic resistance, and treatment responsiveness.[17] Surface modification with targeted ligands is commonly used to ensure the efficient delivery of CeO_2 NPs to cancer cells.[18–20] Riboflavin (Rf), a water-

[a]*Department of Biochemistry, Faculty of Science, Mahidol University, Bangkok, 10400, Thailand. E-mail: anongnat.won@gmail.com; nuchpun.s@gmail.com; napasorn.taa@student.mahidol.edu; kanlaya.pra@mahidol.ac.th*

[b]*Department of Chemistry, Faculty of Science, Kasetsart University, Bangkok, 10900, Thailand. E-mail: fscipplu@ku.ac.th*

[c]*Center for Advanced Studies in Nanotechnology for Chemical, Food and Agricultural Industries, KU Institute for Advanced Studies, Kasetsart University, Bangkok, 10900, Thailand*

[d]*Department of Food Technology, Faculty of Science, Chulalongkorn University, Bangkok, 10330, Thailand. E-mail: sarisa.s@chula.ac.th*

[e]*Department of Community Nursing, Faculty of Nursing, Saint Louis College, Bangkok, 10120, Thailand. E-mail: jintana.a@slc.ac.th*

soluble molecule essential for cellular metabolism, can serve as a dual-function ligand due to its selective uptake by riboflavin carrier proteins, which are frequently overexpressed in several cancer types, including breast cancer.[21–24] Furthermore, Rf exhibits photoreactive properties that can generate ROS upon activation with ultraviolet (UV) or blue light, making it attractive for photodynamic therapy (PDT).[25,26] Therefore, Rf-functionalized CeO_2 NPs (Rf–CeO_2 NPs) might offer photo-induced cytotoxicity *via* ROS generation.

Recent studies have demonstrated that Rf-conjugated nanocarriers improved cellular delivery in breast cancer cells[27–30] and enhanced therapeutic efficacy when combined with light activation.[31] However, the integration of Rf with redox-activated nanoceria for PDT remains unexplored, particularly as a treatment for TNBC. Therefore, combining the redox cycling properties of CeO_2 NPs with Rf photoactivation presents a unique strategy for selectively amplifying oxidative stress in cancer cells. In this study, we performed the synthesis and characterization of Rf–CeO_2 NPs and investigated their light-activated cytotoxic potential in MDA-MB-231 TNBC cells. We hypothesized that Rf modification enhances both cellular uptake and photodynamic efficacy, resulting in increased ROS generation and cancer cell apoptosis under UV irradiation. The results would facilitate the development of a multifunctional nanoplatform for targeted and light-responsive breast cancer therapy.

2. Experimental section

2.1 Materials

Cerium(III) nitrate hexahydrate ($Ce[NO_3]_3 \cdot 6H_2O$), sodium hydroxide (NaOH) pellets, Rf, 3-aminopropyl triethoxysilane (APTES), *N*-hydroxysuccinimide (NHS), and *N*-(3-dimethylaminopropyl)-*N*′-ethylcarbodiimide hydrochloride (EDC) were obtained from Sigma-Aldrich (Burlington, MA, USA). Tri-sodium citrate dihydrate was purchased from Merck (Darmstadt, Germany). Citric acid was purchased from Vidhyasom Co. Ltd (Bangkok, Thailand). Sodium chloride (NaCl), di-sodium hydrogen phosphate dihydrate (Na_2HPO_4), potassium chloride (KCl), potassium dihydrogen phosphate (KH_2PO_4), and absolute ethanol (EtOH) were obtained from VWR Chemicals® (Radnor, PA, USA). 3-(4,5-Dimethylthiazol-2-yl)-2,5-diphenyltetrazolium bromide (MTT) was obtained from PanReac AppliChem, AppliChem GmbH (Darmstadt, Germany). The DCFDA/H2DCFDA Cellular ROS Assay Kit (Abcam, ab113851) was obtained from Merck. The JC-1 MitoMP Detection Kit was purchased from Dojindo (Kumamoto, Japan). Dulbecco's Modified Eagle's Medium (DMEM), minimum essential medium, fetal bovine serum (FBS), horse serum, and penicillin–streptomycin, and dimethyl sulfoxide (DMSO) were supplied by Thermo Fisher Scientific Inc. (Waltham, MA, USA).

2.2 Methods

2.2.1 Synthesis of CeO_2 NPs. To synthesize CeO_2 NPs, $Ce(NO_3)_3$ $6H_2O$ was dissolved in deionized water to achieve a final concentration of 0.1 M. The dispersed solution was stirred at 50 °C for 20 min to ensure complete dissolution and homogeneity. The solution was subsequently adjusted to pH 12 by adding 1 M NaOH solution dropwise. The reaction mixture was maintained at 50 °C under constant stirring for 24 h to facilitate NP formation and growth. After completion, the NP suspension was purified by adding ethanol and centrifuged at 14 352 × *g* for 30 min until a white precipitate was obtained. The precipitate was then washed several times with deionized water until the supernatant reached pH 7, after which it was filtered. The collected CeO_2 NPs were then freeze-dried and further calcined in a muffle furnace at 400 °C for 2 h. The as-prepared samples were sealed and stored under vacuum until further use.

2.2.2 Synthesis of amine-functionalized CeO_2 NPs. Amine-functionalized CeO_2 NPs (NH_2–CeO_2 NPs) were synthesized as described previously.[32] Briefly, 500 mg CeO_2 NPs were dispersed in 50 mL deionized water under vigorous stirring to ensure uniform dispersion. Next, 1 mL APTES was gradually added to the mixture. The reaction mixture was subjected to constant stirring and refluxed at 76 °C for 12 h to facilitate functionalization. After the reaction, the resulting mixture was centrifuged (2254 × *g*, 4 °C, 10 min) to separate the solid product from the supernatant. The collected white solid was washed twice with 10 mL ethanol to remove any unreacted APTES. Each washing step was followed by centrifugation (2254 × *g*, 4 °C, 5 min) to ensure thorough purification. Finally, the purified solid product was dried overnight at 50 °C to obtain the NH_2–CeO_2 NP powder.

2.2.3 Synthesis of Rf–CeO_2 NPs. Rf molecules were functionalized onto NH_2–CeO_2 NPs by amidation. The carboxylic groups in Rf–citrate ester (CARf) were coupled with the amino groups of NH_2–CeO_2 NPs using the EDC–NHS coupling reaction (Fig. 1). Initially, 50 mg CARf was dissolved in 25 μL DMSO and stirred at room temperature for 30 min. Subsequently, 40 mg NHS and 40 mg EDC were added to the solution and stirred at room temperature. In a separate step, 100 mg NH_2–CeO_2 NPs were dispersed in 10 μL deionized water to prepare a dispersed NP solution, which was subsequently added to the preactivated CARf reaction mixture. Then, the conjugation process was initiated under stirring at room temperature for 24 h. After the reaction was completed, the solution was purified by centrifugation (2254 × *g*, 4 °C, 10 min) and washed with DMSO to obtain a yellow solid product. The product was washed with DMSO at least two more times or until a clear supernatant was obtained. Finally, the product was washed with deionized water and centrifuged before being dried overnight at 50 °C to obtain conjugated CeO_2–NH_2–CARf NPs, which were stored at room temperature until characterization. The conjugated CeO_2–NH_2–CARf NPs were then characterized by fluorescence spectroscopy (RF-5301 PC Spectrofluorophotometer, Shimadzu, Japan) to confirm the successful attachment of the fluorophore and assess its optical properties. The percent mass recovery of NH_2–CeO_2, Rf–CeO_2, and overall yield were calculated according to the equation:

$$\%\ \text{mass recovery} = \frac{\text{final mass}}{\text{initial mass}} \times 100$$

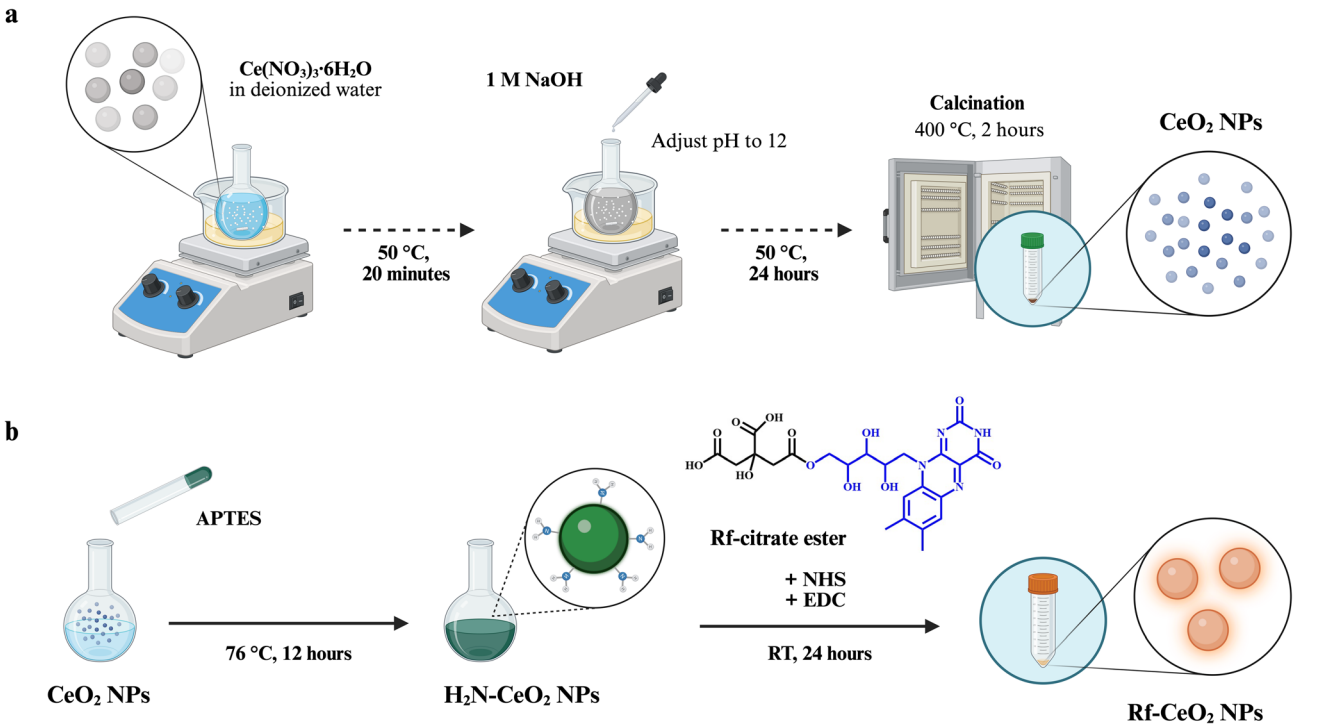

Fig. 1 Schematic illustration of the synthesis and riboflavin (Rf) functionalization of cerium oxide nanoparticles (CeO_2 NPs). (a) CeO_2 NPs were synthesized *via* precipitation by reacting cerium nitrate hexahydrate ($Ce[NO_3]_3 \cdot 6H_2O$) with 1 M NaOH in deionized water, adjusting the pH to 12, and incubating at 50 °C for 24 h. The resulting precipitate was collected and calcined at 400 °C for 2 h to obtain CeO_2 NPs. (b) CeO_2 NPs were functionalized with (3-aminopropyl)triethoxysilane (APTES) at 76 °C for 12 h to obtain amine-modified CeO_2 (H_2N-CeO_2) NPs. These were further conjugated with Rf–citrate ester in the presence of 1-ethyl-3-(3-dimethylaminopropyl)carbodiimide (EDC) and *N*-hydroxysuccinimide (NHS) at room temperature for 24 h to produce Rf-functionalized CeO_2 (Rf–CeO_2) NPs.

2.2.4 Characterization of the synthesized NPs

2.2.4.1 Dynamic light scattering measurement. The hydrodynamic diameter and zeta potential of the synthesized NPs were analyzed by dynamic light scattering (DLS). Both measurements were performed with a Zetasizer Ultra (Malvern Panalytical) at a controlled temperature of 25 °C to ensure consistency. To optimize the measurement accuracy and minimize interference, the NP samples were diluted with deionized water as the dispersion medium at a 1 : 100 ratio for a final NP concentration of 0.1 mg mL^{-1}.

2.2.4.2 Transmission electron microscopy analysis. The morphological characteristics and structural integrity of the NPs were visualized by transmission electron microscopy (TEM) with a JEM-3100 (HR) instrument. Prior to imaging, the NPs were redispersed in ethanol at a concentration of 0.5 mg mL^{-1} to facilitate uniform sample deposition. The sample was prepared by placing a small droplet of the NP dispersion onto a carbon-supported copper grid (TEM grid, PELCO, TED PELLA) and allowing it to dry under ambient conditions.

2.2.4.3 Field emission scanning electron microscopy analysis. The morphology and size of the synthesized NPs were determined using a field emission scanning electron microscope (FESEM, FEI Quanta 450). The samples were prepared by placing the NPs on a carbon-coated copper grid, and the NPs were then gold-coated to improve the conductivity.

2.2.4.4 Fourier transform infrared spectroscopy analysis. The Fourier-transform infrared (FTIR) spectra of the synthesized CeO_2 NPs were recorded by FTIR spectroscopy (Bruker Tensor 27) to analyze their vibrational characteristics and confirm the presence of functional groups. The spectra were collected over a broad wavenumber range of 4000–500 cm^{-1} with 32 scanning times at a resolution of 4 cm^{-1} to enable the identification of key absorption bands associated with the chemical structure and phase composition of the NPs. This analysis provides valuable insights into the bonding environment and structural integrity of the synthesized CeO_2 NPs.

2.2.4.5 Powder X-ray diffraction. The crystalline structure of the synthesized CeO_2 NPs was analyzed using a benchtop X-ray diffractometer (Bruker D8 Advance XRD) at 40 kV, 40 mA using CuKα as a light source. X-ray diffraction (XRD) patterns were obtained by scanning over a 2θ range of 20°–90° using a copper Kα radiation source with a wavelength of 1.5418 Å.

2.2.5 Cell culture. The TNBC cell line MDA-MB-231 (HTB-26) and normal breast epithelial cells MCF-10A were obtained from ATCC. MDA-MB-231 cells were cultured in DMEM with 10% FBS and 1% penicillin–streptomycin, while MCF-10A cells were maintained in DMEM/F12 with horse serum and insulin (Gibco, UK). EGF and hydrocortisone were from Sigma-Aldrich and HiMedia (Mumbai, India), respectively. Cells were incubated at 37 °C in 5% CO_2.

2.2.6 Cell viability and photodynamic therapy assays. The cytotoxicity of the NPs was evaluated using the 3-(4,5-dimethyl-2-thiazolyl)-2,5-diphenyl-2*H*-tetrazolium bromide (MTT) assay. Cells were seeded in 96-well plates (8×10^3 cells per well) and

incubated for 24 h at 37 °C with 5% CO_2. The cells were treated with complete medium containing either CeO_2 or Rf–CeO_2 with final drug concentrations of 25, 50, 100, 200, 400, and 600 μg mL^{-1} under dark conditions and 6.25, 12.5, 25, 50, 100, and 200 μg mL^{-1} under photodynamic conditions. After 90 min incubation, the cells were irradiated with UV-A light for 10 min using a UV nail lamp (power density = 3.95 mW cm^{-2}) and cultured further for 48 h. After treatment, the culture medium was discarded and replaced with MTT solution (0.5 mg mL^{-1} in serum-free medium), followed by 4 h of incubation at 37 °C. The MTT solution was then removed, and 100 μL DMSO was added to each well to solubilize the formazan crystals. The absorbance was measured at 540 nm using a microplate reader (Thermo Fisher Scientific, Wilmington, DE, USA). Cell viability was expressed as the percentage relative to the untreated controls and was calculated according to the equation:

$$\%\ \text{cell viability} = \frac{\text{absorbance of treated} - \text{absorbance of blank}}{\text{absorbance of control} - \text{absorbance of blank}} \times 100$$

All experiments were conducted in triplicate with at least three independent repeats to ensure reproducibility.

2.2.7 Intracellular ROS generation. Intracellular ROS levels were quantified using the DCFDA/H2DCFDA Cellular ROS Assay Kit (Abcam, ab113851) following the manufacturer's protocol. MDA-MB-231 cells were seeded into black 96-well plates at a density of 2.5×10^4 cells per well and incubated overnight at 37 °C with 5% CO_2 to facilitate cell attachment. The following day, the cells were washed with the provided 1× assay buffer and incubated with 25 μM DCFDA solution (prepared in 1× buffer) for 45 min at 37 °C in the dark. After incubation, excess dye was removed by washing the cells with 1× buffer. The cells were then treated with CeO_2 or Rf–CeO_2 NPs at concentrations of 25, 50, 100, and 200 μg mL^{-1}. To evaluate the photodynamic effect, cells were incubated for 90 min, exposed to UV-A light for 10 min using a UV nail lamp, and then incubated for 24 h under standard culture conditions. The fluorescence intensity, which indicates intracellular ROS generation, was measured using a fluorescence microplate reader at an excitation/emission wavelength of 485/535 nm. The relative fluorescence units were normalized based on the untreated controls. The Operetta High Content Imaging System (PerkinElmer, Waltham, MA, USA) was used to capture fluorescent signals. All experiments were performed in triplicate and repeated independently at least three times.

2.2.8 Mitochondrial membrane potential assay. Mitochondrial membrane potential (MMP) was measured using the JC-1 assay (Dojindo Laboratories, Japan) according to the manufacturer's protocol. MDA-MB-231 cells were seeded in 96-well black, clear-bottom plates at a density of 2.5×10^4 cells per well and incubated overnight at 37 °C in a 5% CO_2 atmosphere to facilitate cell attachment. Following treatment with CeO_2 or Rf–CeO_2 NPs (at 25, 50, 100, and 200 μg mL^{-1}) for 48 h, with or without UV-A irradiation (10 min, 3.95 mW cm^{-2}) after 90 min pre-incubation, the cells were incubated with 4 μM JC-1 dye in serum-free medium for 60 min at 37 °C in the dark. After incubation, the cells were washed twice with 1× assay buffer to remove excess dye. Fluorescence was measured using a fluorescence microplate reader (Agilent Technologies, USA) at excitation/emission wavelengths of 485/530 nm for JC-1 monomers (green) and 535/590 nm for JC-1 aggregates (red). The red/green fluorescence intensity ratio was calculated to measure the changes in the MMP. A decrease in the red/green fluorescence ratio indicates a loss of MMP and mitochondrial depolarization. Fluorescence imaging was performed with the Operetta High Content Imaging System (PerkinElmer, Waltham, MA, USA).

3. Results

3.1 Characterization of CeO_2 and Rf–CeO_2 NPs

CeO_2 particles appeared as white powder, whereas Rf–CeO_2 showed as yellow clumped powder (Fig. 2a and d, respectively). The morphology, shape, and structural arrangement of both NPs were examined. The surface morphology and distribution of both NPs were investigated by SEM, as shown in (Fig. 2b and e). The SEM image of CeO_2 in Fig. 2b reveals a relatively uniform dispersion of rod-like NPs. The particles appear to be densely packed with slight aggregation. After Rf functionalization (Fig. 2e), the particles became slightly more textured and less aggregated. The obtained TEM images confirmed the SEM results that both CeO_2 and Rf–CeO_2 exhibited a rod-shaped morphology and a clustered arrangement (Fig. 2c and f, respectively). To evaluate the synthesis efficiency for Rf–CeO_2 NPs, mass recovery was determined after each modification step. Starting with 500 mg of CeO_2, the amination step yielded 545.6 mg of NH_2–CeO_2 (109.1% mass recovery), indicating successful attachment of amine ligands to the nanoparticle surface. Conjugation of 100 mg NH_2–CeO_2 with riboflavin produced 88.9 mg of Rf–CeO_2 (88.9% mass recovery). Since these processes involve surface functionalization rather than molecular synthesis, reaction efficiency was expressed as the mass recovery of dried products. Overall, the process achieved a high total mass recovery (~97%), demonstrating efficient functionalization of CeO_2 with riboflavin. The hydrodynamic size of CeO_2 NPs was measured by DLS (Table 1). CeO_2 NPs were larger than Rf–CeO_2 NPs, which might be because CeO_2 tends to form aggregates in the aqueous solution. Upon Rf modification, the NP surfaces became more stable, resulting in a significantly lower average particle size and a narrower size distribution. The size distribution of CeO_2 and Rf–CeO_2 was also assessed. The majority of unmodified CeO_2 NPs were distributed within the 100–500 nm range, reflecting moderate polydispersity (Fig. S1a). In comparison, Rf–CeO_2 nanoparticles exhibited a more uniform distribution, with about 65–75% of the particles falling within the 100–400 nm range (Fig. S1b). This enhanced stability is further indicated by the zeta potential measurements. While CeO_2 exhibited a negative zeta potential due to surface hydroxyl groups, the surface charge became positive after Rf functionalization, indicating successful functionalization, as Rf contains positively charged functional groups. Moreover, the positive surface charge likely contributed to the increased electrostatic repulsion between particles, thereby minimizing aggregation and promoting a more stable suspension.

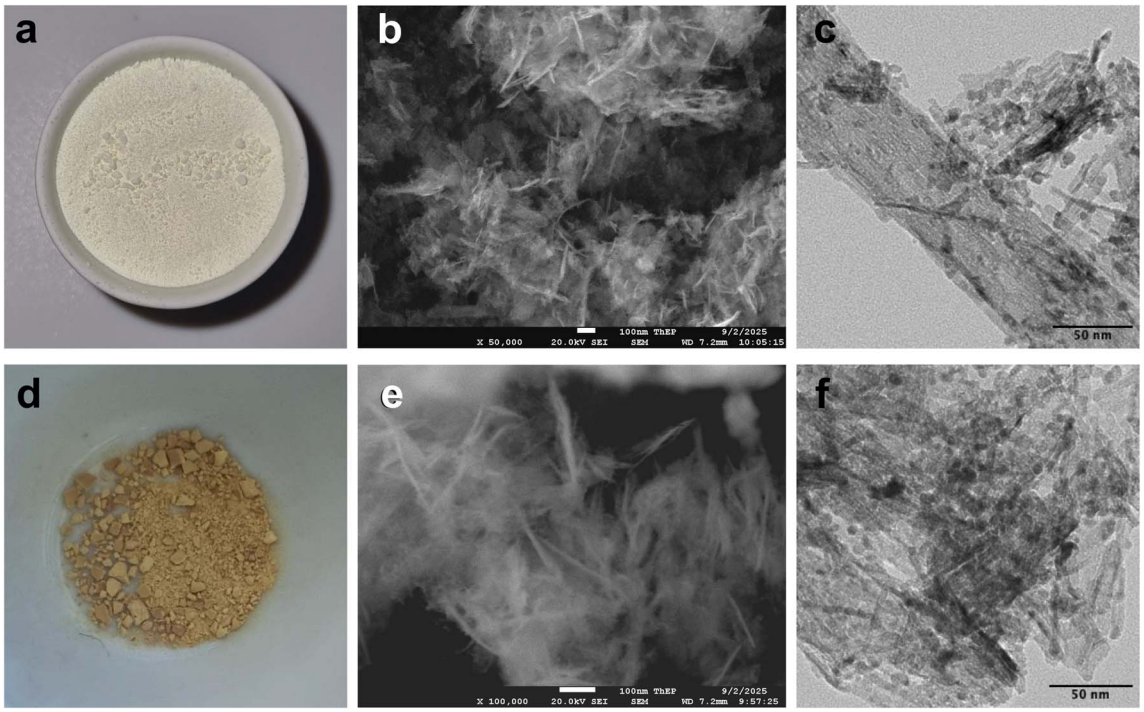

Fig. 2 Characterization of CeO_2 and Rf–CeO_2 NPs. (a) CeO_2 and (d) Rf–CeO_2. Field-emission scanning electron microscopy images of CeO_2 (b) and Rf–CeO_2 (e). Transmission electron microscopy images of CeO_2 (c) and Rf–CeO_2 (f). Both NPs exhibit a well-defined, rod-shaped morphology with an average particle size of < 50 nm.

Table 1 D_H and zeta potential of CeO_2 and Rf–CeO_2 NPs[a]

Nanoparticles	D_H (nm)	PDI	Zeta potential (mV)
CeO_2	436.7 ± 92.91	0.48 ± 0.07	−22.3
Rf–CeO_2	363.7 ± 15.21	0.50 ± 0.03	28.6

[a] Hydrodynamic diameter (D_H), polydispersity index (PDI).

3.2 Fluorescence, FTIR, and XRD analyses of CeO_2 and Rf–CeO_2

To functionalize Rf onto CeO_2 NPs, Rf–citrate ester (CARf) was used to modify CeO_2 NPs. The structures of Rf and CARf are shown in Fig. 3a. Fluorescence spectroscopy was performed to confirm the successful conjugation of the Rf–citrate ester (CARf) onto the CeO_2 NPs (Fig. 3b). The CARf exhibited a strong emission peak centered at 520 nm, which is characteristic of its isoalloxazine ring system.[33] Rf–CeO_2 retained this fluorescence signal, confirming the presence of Rf on the NP surface. In contrast, unfunctionalized CeO_2 NPs exhibited negligible fluorescence in the same region, indicating the absence of Rf. The FTIR spectra of CeO_2, CARf, and Rf–CeO_2 NPs are shown in Fig. 3c. In the spectrum for the CeO_2 sample, the peak at 3400 cm^{-1} corresponded to the –OH stretching vibrations of the hydroxyl groups, while in the modified sample, the –NH stretching of the amide overlapped with the –OH stretching, which appeared at around the same frequency (3200–3600 cm^{-1}).[34] CARf shows characteristic peaks at ~3400–3200 cm^{-1} (O–H/N–H), ~2925–2850 cm^{-1} (C–H), ~1680–1640 cm^{-1} (C═O/C═N), and ~1200 cm^{-1} (C–N/C–O). The distinct bands observed around 1300–1500 cm^{-1} in the Rf–CeO_2 spectrum were associated with the C–H bending of the CARf structure and C–N stretching of the aromatic amines from Rf, which also exhibited major peaks at 1743 cm^{-1} corresponding to the C═O bonds in the Rf structure. Furthermore, the presence of an amide linkage was identified. The peaks noted at 1692 and 1530 cm^{-1} correspond to the C═O amide and C–N bond stretching,[35] confirming the successful Rf functionalization of CeO_2 NPs.

Furthermore, the frequency bands at 850 and 540 cm^{-1} are attributed to the Ce–O stretching observed in both CeO_2 and Rf–CeO_2 NP samples, indicating the presence of CeO_2 NPs and their derivatives. The FTIR spectra of Rf–CeO_2 indicated the presence of major peaks from Rf, which were absent in the spectrum of unmodified CeO_2, confirming the successful functionalization of Rf onto CeO_2. The XRD patterns of CeO_2 and Rf–CeO_2 NPs are presented in Fig. 3d. Both samples revealed a series of sharp and intense diffraction peaks located at approximately $2\theta = 28.5°$, 33.1°, 47.5°, 56.3°, 59.1°, and 69.4°, which correspond to the (111), (200), (220), (311), (222), and (400) crystal planes of CeO_2 (JCPDS no. 34-0394), respectively. No significant shifts were observed in the peak positions after functionalization, indicating that the crystalline structure of CeO_2 remained intact. However, the intensity of the Rf–CeO_2 peaks increased slightly and became more well-defined, possibly due to improved crystallinity or reduced aggregation after surface modification. Moreover, using the Debye–Scherrer equation from the (111) plane, the approximate crystallite size of CeO_2 NPs was calculated to be 436.7 nm, which indicates good agreement with the TEM results. Furthermore, the absence of any new peaks indicates that Rf was coated onto the CeO_2 surface in an amorphous or noncrystalline form.

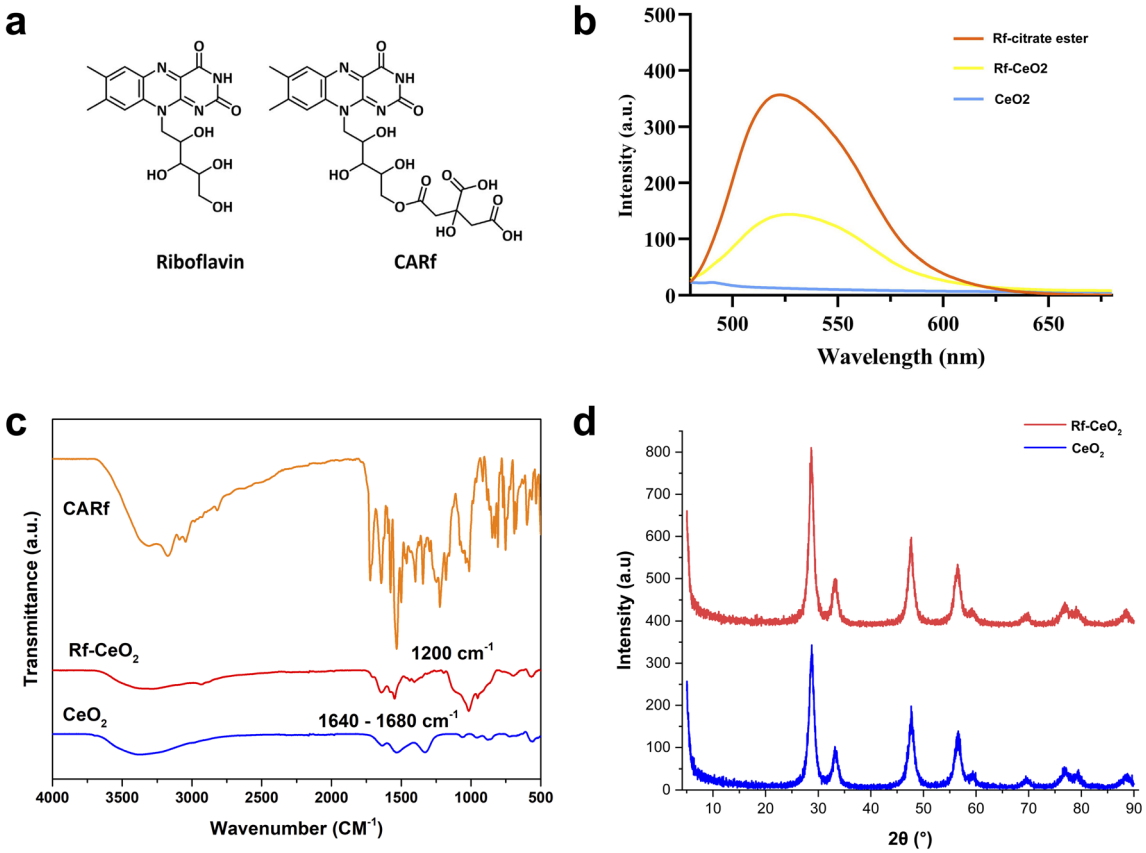

Fig. 3 Fluorescence, Fourier-transform infrared (FTIR) spectroscopy, and X-ray diffraction (XRD). (a) Structures of riboflavin (Rf) and Rf–citrate ester (CARf); (b) fluorescence intensity of CARf (red), Rf–CeO_2 NPs (yellow), and CeO_2 NPs (blue); (c) FTIR spectra and (d) XRD patterns of Rf–CeO_2 (red) and CeO_2 NPs (blue).

3.3 Cytotoxicity of CeO_2 and Rf–CeO_2 NPs in MDA-MB-231 cells

The cytotoxicity of CeO_2 and Rf–CeO_2 NPs on MDA-MB-231 cells was assessed using the MTT assay. The result revealed a dose-dependent decrease in cell viability in both NPs compared with the control group. However, the half maximal inhibitory concentration (IC_{50}) of CeO_2 on breast cancer cells in 48 h is non-applicable since the maximum concentration of 600 μg mL^{-1} cannot reduce cancer cell viability to 50%. In contrast, MDA-MB-231 cells treated with Rf–CeO_2 NPs exhibited an IC_{50} of 57.71 ± 0.04 μg mL^{-1} (Fig. 4a). Thus, Rf–CeO_2 NPs exhibited more potent cytotoxic effects on MDA-MB-231 cells than CeO_2 NPs alone. The bar graph in Fig. 4b compares the percentage of cell viability of MDA-MB-231 after treatment between CeO_2 and Rf–CeO_2 NPs at each concentration. The results are plotted on the IC_{50} value line graph, in which the viability of MDA-MB-231 cells treated with Rf–CeO_2 NPs was significantly lower than that of those treated with CeO_2 NPs in every concentration. Therefore, Rf–CeO_2 NPs exert more potent cytotoxicity against breast cancer cells than CeO_2 NPs.

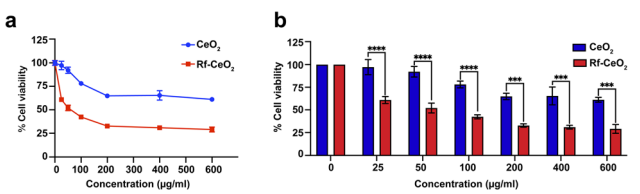

Fig. 4 The anti-cancer effect of CeO_2 or Rf–CeO_2 NPs on MDA-MB-231 cells. (a) The half maximal inhibitory concentration value and inhibitory curve. (b) The bar graph of cell viability percentage in MDA-MB-231 cells. Data are expressed as mean ± standard error of the mean ($n = 3$). ***$p < 0.001$, and ****$p < 0.0001$ relative to the control, two-way analysis of variance.

3.4 Cytotoxicity of UV-irradiated CeO_2 and Rf–CeO_2 NPs in MDA-MB-231 cells

To evaluate the effects of UV-activated CeO_2 and Rf–CeO_2 NPs on MDA-MB-231 TNBC cells, cytotoxicity, intracellular ROS generation, and MMP were assessed following 10 min of UV exposure after incubation for 90 min. The cytotoxic potential of CeO_2 and Rf–CeO_2 after UV exposure was assessed using the MTT assay. The results are presented in Fig. 5a. Both NPs induced a dose-dependent reduction in cell viability compared with the untreated control. However, even after UV exposure, CeO_2 was unable to achieve IC_{50} at any concentration (6.25, 12.5, 25, 50, 100, and 200 μg mL^{-1}). In contrast, Rf–CeO_2 demonstrated significantly enhanced cytotoxicity, with an IC_{50} value of 39.9 ± 0.07 μg mL^{-1} after 48 h. Furthermore, the IC_{50} of UV-irradiated Rf–CeO_2 treatment was lower than that of Rf–CeO_2 without UV exposure (IC_{50} = 57.71 ± 0.04 μg mL^{-1};

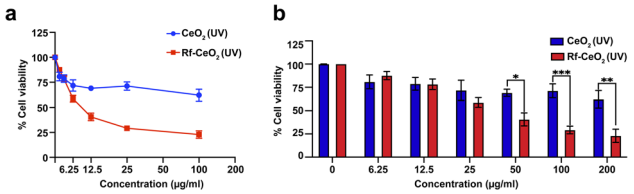

Fig. 5 Cytotoxic effects of UV-activated CeO_2 and Rf–CeO_2 NPs on MDA-MB-231 cells. Cells were treated with CeO_2 or Rf–CeO_2 NPs for 48 h following 10 min of UV exposure. (a) The line graph depicts the IC_{50} values, showing a markedly lower IC_{50} for Rf–CeO_2 compared with CeO_2. (b) The bar graph presents the mean ± standard error of the mean cell viability percentage. Data are expressed as mean ± standard error of the mean ($n = 3$). *$p < 0.05$, **$p < 0.01$, and ***$p < 0.001$ relative to control, two-way analysis of variance.

Fig. S2a). This reduction in IC_{50} upon UV activation highlights the photodynamic enhancement of Rf–CeO_2-mediated cytotoxicity. Consistent with these findings, the bar graph analysis of cell viability across various concentrations in Fig. 5b confirmed that Rf–CeO_2 consistently induced greater cytotoxic effects than CeO_2. These results indicate that UV activation, particularly in Rf–CeO_2, enhanced the cytotoxic activity of CeO_2 NPs. Although UV activation enhanced the overall potency of Rf–CeO_2, no significant difference in cell viability was observed between the irradiated and non-irradiated Rf–CeO_2 treatments at individual concentrations (Fig. S2b). These results collectively signify that Rf–CeO_2 NPs exhibited even greater cytotoxicity after further potentiation by UV-induced photodynamic activation. The cytotoxicity of Rf–CeO_2 was also investigated in normal breast cells (MCF-10A). The IC_{50} of Rf–CeO_2 on MCF-10A cells after 48 h was 12.06 ± 0.04 μg mL^{-1} (Fig. S3a), which was notably lower than the IC_{50} for breast cancer cells (MDA-MB-231). After 10 min of UV exposure, the IC_{50} decreased further to 5.81 ± 0.05 μg mL^{-1} (Fig. S3b). A direct comparison of cell viability between UV-exposed and non-exposed groups at each concentration is shown in Fig. S3c. These findings indicate that Rf–CeO_2 exhibits cytotoxic effects on normal breast cells both with and without UV exposure. However, strategies such as tumor-targeted delivery, cancer-specific surface functionalization, or localized UV irradiation could improve tumor accumulation of Rf–CeO_2, thereby reducing off-target effects and enhancing its safety and efficacy for cancer therapy.

3.5 Intracellular ROS generation assessed using the DCFDA fluorescence assay

Based on the well-established redox mechanism of cerium oxide nanoparticles (CeO_2 NPs), which involves cycling between Ce^{3+} and Ce^{4+} oxidation states and consequent enhancement of ROS generation selectively in cancer cells, intracellular ROS levels in MDA-MB-231 cells treated with either CeO_2 or Rf–CeO_2 NPs were assessed using the DCFDA fluorescence assay. The intracellular ROS levels in MDA-MB-231 cells were evaluated using DCFDA staining after treatment with CeO_2 or Rf–CeO_2 NPs at concentrations of 25, 50, 100, and 200 μg mL^{-1}, with or without UV exposure for 10 min. In the absence of UV exposure, CeO_2 treatment did not alter the fluorescence intensity across several concentrations. In contrast, Rf–CeO_2-treated cells dose-dependently exhibited increasing green fluorescence intensity at markedly higher rates than those in CeO_2-treated cells, indicating elevated intracellular ROS generation following Rf functionalization. Upon UV activation, both CeO_2 and Rf–CeO_2 NPs showed increased green fluorescence; however, the enhancement was substantially greater in the Rf–CeO_2 group, verifying the photodynamic activation of Rf under UV light. Furthermore, a direct comparison between cells treated with Rf–CeO_2 alone and those treated with Rf–CeO_2 and subsequent UV exposure revealed a significant difference in the increase in green fluorescence intensity in the UV-irradiated group, particularly at 100 and 200 μg mL^{-1} (Fig. 6a). These findings are consistent with the results of the DCFDA fluorescence assay for measuring intracellular ROS using a microplate reader (excitation/emission: 485/535 nm). Rf–CeO_2 treatment resulted in a more significant, dose-dependent increase in ROS levels compared with untreated control cells (Fig. 6b). Rf–CeO_2 treatment at all concentrations induced markedly higher DCFDA fluorescence intensity than CeO_2 treatment, which exhibited minimal ROS generation with no significant difference from the control group. These findings indicate that Rf functionalization enhances the oxidative potential of CeO_2 NPs. The elevated ROS levels observed in Rf–CeO_2-treated cells are likely associated with the more potent cytotoxicity of Rf–CeO_2 than that of CeO_2. Furthermore, excessive intracellular ROS can damage cellular components and trigger apoptotic pathways. These results demonstrate that Rf–CeO_2 can increase intracellular ROS production than CeO_2. UV-irradiated Rf–CeO_2 elicited a significant, dose-dependent increase in DCFDA fluorescence intensity, indicating higher intracellular ROS production than that in the untreated control and CeO_2-treated cells. UV-irradiated CeO_2 did not significantly alter ROS levels compared with the control. At equivalent concentrations (50, 100, and 200 μg mL^{-1}), Rf–CeO_2 induced significantly higher intracellular ROS generation than CeO_2, indicating that Rf functionalization enhanced oxidative stress, particularly with UV activation (Fig. 6c). These findings are consistent with the observed cytotoxicity, indicating that ROS generation plays a key role in the enhanced antitumor activity of Rf–CeO_2. Furthermore, comparison of the DCFDA fluorescence intensity revealed that Rf–CeO_2 NPs subjected to UV exposure increased ROS generation by approximately two-fold at concentrations of 100 and 200 μg mL^{-1} compared with non-irradiated Rf–CeO_2 (Fig. S4). This pronounced upregulation of oxidative stress following UV activation underscores the photodynamic properties of the Rf-functionalized CeO_2 NPs. These findings are consistent with the cytotoxicity results, in which UV-irradiated Rf–CeO_2 exhibited greater cytotoxic effects on MDA-MB-231 cells than non-irradiated Rf–CeO_2.

3.6 MMP disruption assessed by JC-1 staining

The enhanced cytotoxicity observed in Rf–CeO_2-treated MDA-MB-231 cells is attributed to elevated intracellular ROS generation. Excessive ROS production impairs mitochondrial function by inducing loss of MMP, an early indicator of apoptosis.

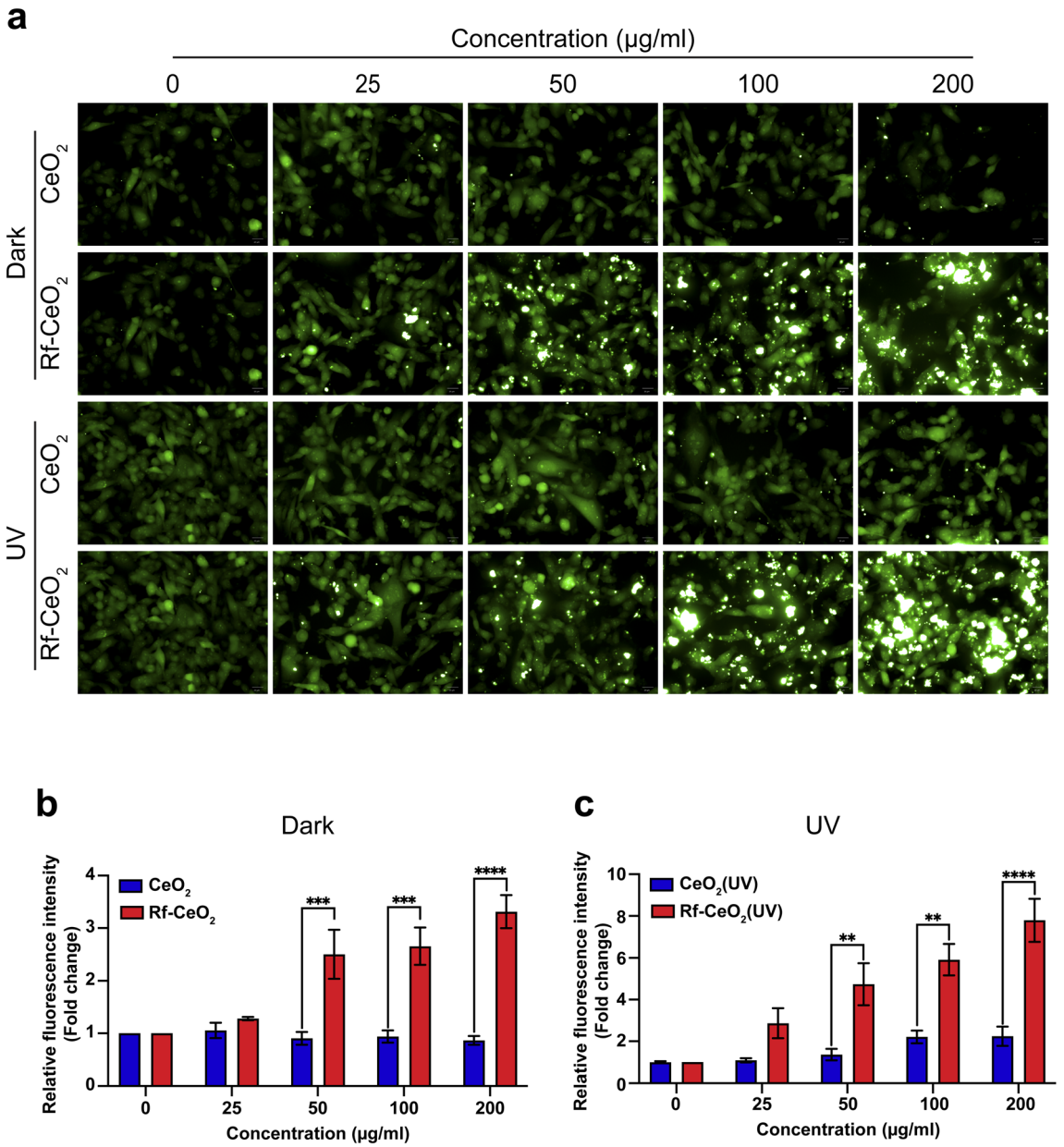

Fig. 6 Measurement of intracellular reactive oxygen species (ROS) levels using the DCFDA fluorescence assay. (a) Cells were treated with either CeO_2 or Rf–CeO_2 NPs at concentrations of 25, 50, 100, and 200 μg mL^{-1} for 24 h, with or without subsequent UV exposure (10 min). Then, DCFDA staining in MDA-MB-231 cells was visualized by Operetta high-content imaging. Relative fluorescence intensity of DCFDA dye was analyzed using a microplate reader after treating cells with either CeO_2 or Rf–CeO_2 NPs at concentrations of 25, 50, 100, and 200 μg mL^{-1} for 24 h, without (b) or with subsequent UV exposure (c). Data are represented as fold change, mean ± standard error of the mean ($n = 3$). $^{**}p < 0.01$, $^{***}p < 0.001$, and $^{****}p < 0.0001$ relative to the control, two-way analysis of variance.

The MMP in MDA-MB-231 cells was evaluated using JC-1 dye following treatment with CeO_2 or Rf–CeO_2 NPs at concentrations of 25, 50, 100, and 200 μg mL^{-1}, with or without UV exposure. JC-1 is a cationic lipophilic dye that selectively accumulates in mitochondria in a MMP-dependent manner. In healthy, polarized mitochondria, JC-1 forms aggregates that emit red fluorescence. Conversely, in depolarized or dysfunctional mitochondria, JC-1 remains in its monomeric form in the cytoplasm, emitting green fluorescence. Therefore, the red/green fluorescence intensity ratio is a sensitive indicator of mitochondrial integrity, with a decrease in the ratio indicating early apoptosis.

In the non-UV-treated groups, CeO_2-treated cells exhibited no noticeable change in red or green fluorescence compared with untreated controls, indicating preserved mitochondrial membrane potential. In contrast, Rf–CeO_2 treatment dose-dependently increased green fluorescence, with a corresponding decrease in red fluorescence (Fig. S5a), indicating progressive mitochondrial depolarization. This shift in JC-1 staining appeared as merged images dominated by green fluorescence

(Fig. 7a), further supporting the loss of MMP with increasing NP concentration. Following 10 min of UV exposure, Rf–CeO_2 induced a dose-dependent increase in green fluorescence with a concurrent reduction in red fluorescence (Fig. S5b), producing merged images prominently dominated by the green signal, especially at higher concentrations (100 and 200 μg mL^{-1}). This observation confirms the role of Rf in enhancing photodynamic activity and promoting MMP disruption. These data are consistent with the microplate reader-based JC-1 assay results. This assay relies on the red/green fluorescence intensity ratio as an indicator of mitochondrial polarization, where red fluorescence (excitation/emission: 535/595 nm) indicates healthy, polarized mitochondria, whereas green fluorescence (excitation/emission: 485/535 nm) indicates depolarized, dysfunctional mitochondria. Cells were treated with CeO_2 or Rf–CeO_2 NPs (25, 50, 100, and 200 μg mL^{-1}) for 48 h. Both NPs induced a dose-dependent reduction in the red/green fluorescence ratio, indicating MMP loss (Fig. 7b).

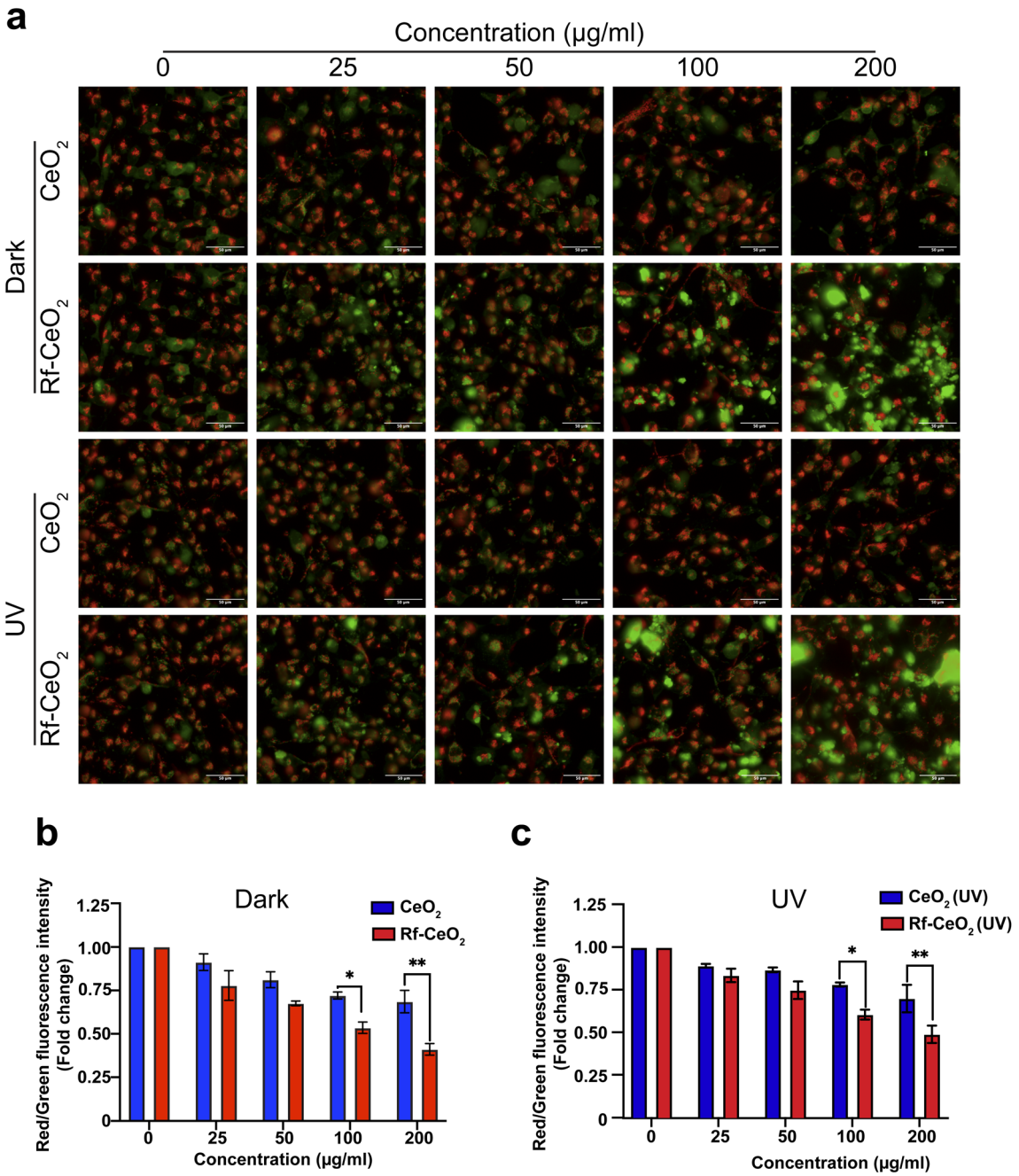

Fig. 7 The assessment of mitochondrial membrane potential in MDA-MB-231 cells using JC-1 dye after treatment with CeO_2 or Rf–CeO_2 nanoparticles (25, 50, 100, and 200 μg mL^{-1}) with or without 10 min of UV exposure. (a) Fluorescence images of JC-1 dye staining. Images were captured using high-content Operetta imaging. Scale bar = 50 μm. Red/green fluorescence intensity ratio was analyzed using a microplate reader without (b) or with subsequent UV exposure (c). Data are represented as fold change, mean ± standard error of the mean ($n = 3$). *$p < 0.05$, and **$p < 0.01$, relative to the control, two-way analysis of variance.

However, Rf–CeO_2 treatment resulted in a significantly greater decrease in MMP than CeO_2, particularly at higher concentrations (100 and 200 μg mL^{-1}). This marked reduction in mitochondrial polarization in the Rf–CeO_2-treated group demonstrates that Rf functionalization enhanced the ability of CeO_2 to disrupt mitochondrial function. Following treatment with UV-irradiated CeO_2 and Rf–CeO_2, the red/green fluorescence intensity ratio in MDA-MB-231 cells dose-dependently decreased, indicating mitochondrial depolarization. Fig. 7c shows that Rf–CeO_2 treatment significantly reduced the red/green ratio at both 100 and 200 μg mL^{-1} concentrations compared with CeO_2, indicating a stronger disruption of mitochondrial integrity. These data align with the elevated ROS levels and cytotoxic effects observed in the Rf–CeO_2 group and demonstrate the involvement of a redox-mediated apoptotic mechanism.

To investigate whether the UV activation of Rf–CeO_2 further influenced mitochondrial integrity, we compared the red/green fluorescence intensity ratios on JC-1 staining between cells treated with irradiated and nonirradiated Rf–CeO_2. However, no significant differences were observed between the two groups across all tested concentrations (Fig. S5c). These results confirm that Rf–CeO_2 induces greater mitochondrial dysfunction than CeO_2, regardless of UV exposure, which is consistent with the microplate reader-based JC-1 assay results, confirming that Rf–CeO_2 promotes mitochondrial dysfunction more significantly than unmodified CeO_2, possibly through enhanced intracellular ROS generation.

4. Discussion

TNBC presents a significant therapeutic challenge stemming from its aggressive nature and lack of specific molecular targets. Recent studies have investigated redox-modulating nanotherapeutics that are capable of exploiting the higher oxidative stress vulnerability of TNBC cells.[36,37] In this context, CeO_2 NPs, with their unique capacity for redox-switching between Ce^{3+} and Ce^{4+}, have emerged as promising agents. However, their intrinsic anticancer properties remain limited unless further engineered for targeted delivery and enhanced activity.[38–40] In our study, we found that Rf–CeO_2 NPs exert superior anticancer activity compared with unmodified CeO_2 NPs in MDA-MB-231 cells, and this activity is significantly amplified upon UV exposure. Rf–CeO_2 NPs exhibited a markedly lower IC_{50} than CeO_2 NPs, especially with UV activation, indicating enhanced cytotoxic potential. This effect correlates with increased intracellular ROS production and MMP disruption, which are hallmark events of oxidative and mitochondrial stress-induced apoptosis. A key contributor to the enhanced efficacy of Rf–CeO_2 is functionalization with Rf (vitamin B2), a known endogenous photosensitizer. Upon UV irradiation, Rf transitions to an excited triplet state, which can transfer energy to molecular oxygen and generate ROS, particularly singlet oxygen and superoxide radicals.[41,42] This photodynamic mechanism is well-documented and forms the basis for the use of Rf in PDT.[43,44] Rf–CeO_2 NPs generate significantly higher levels of intracellular ROS than CeO_2 NPs, especially after UV exposure, suggesting a synergistic effect between the redox properties of CeO_2 and the photosensitizing effect of Rf. The increase in ROS generation induced by Rf–CeO_2 NPs triggered a substantial dose-dependent loss of MMP, as observed in JC-1 staining. In untreated cells or those treated with CeO_2 NPs, JC-1 formed red-emitting aggregates in healthy mitochondria. In contrast, in cells treated with Rf–CeO_2, green fluorescence increased while red fluorescence decreased, indicating mitochondrial depolarization.[45] These changes were observed regardless of UV exposure, although the UV-exposed cells also increasingly emitted green fluorescence, which is consistent with high ROS accumulation. These findings indicate that although mitochondrial disruption is primarily ROS-mediated, photodynamic enhancement intensifies oxidative damage, likely leading to irreversible apoptotic signalling.

Importantly, our findings also establish that Rf functionalization improves the cellular uptake and tumor selectivity of CeO_2 NPs. Rf binds to Rf transporters (RFVTs), which are often overexpressed in various cancers, including breast cancer.[46] This targeting strategy not only facilitates more efficient NP internalization but may also localize the NPs near the mitochondria, where Rf also naturally accumulates, given its role in oxidative metabolism, thereby enhancing photodynamic disruption directly at the mitochondrial level.[47,48] Together, these underlying mechanisms explain why Rf–CeO_2 NPs are significantly more cytotoxic to breast cancer cells than CeO_2

The combination of active targeting *via* RFVT-mediated uptake, Rf photoactivity, and redox dynamics of CeO_2 can inhibit cancer cell progression in multiple ways: increasing ROS production, impairing mitochondrial function, and initiating apoptosis. Moreover, UV activation further enhanced this cytotoxic cascade, highlighting the potential of Rf–CeO_2 NPs as a novel light-activated nanotherapeutic platform for TNBC. While our findings provide valuable insights into the effects of cerium oxide nanoparticles (CeO_2 NPs) and Rf-functionalized CeO_2 NPs on ROS generation in MDA-MB-231 cells, this study has several limitations. Notably, the long-term cytotoxicity, biodistribution, and potential immunogenicity of the CeO_2 and Rf–CeO_2 nanoparticles were not evaluated. Furthermore, the precise molecular mechanisms responsible for the enhanced reactive oxygen species (ROS) generation observed with Rf–CeO_2 NPs remain to be elucidated. Future studies should explore the role of RFVTs in the uptake of Rf–CeO_2 NPs, investigate their biodistribution and pharmacokinetics *in vivo*, and explore the feasibility of using clinically applicable light sources to activate them. Nonetheless, our data provide a compelling rationale for the continued development of Rf-functionalized nanomaterials as targeted photodynamic agents in cancer therapy.

5. Conclusion

This study demonstrated that Rf–CeO_2 NPs exhibit significantly enhanced cytotoxicity against MDA-MB-231 breast cancer cells compared with unmodified CeO_2 NPs. Although CeO_2 NPs minimally impacted cell viability, Rf–CeO_2 NPs effectively induced ROS generation, reduced MMP, and promoted cancer cell death. Furthermore, UV activation further amplified the

anticancer effect of Rf–CeO_2 NPs, indicating their potential application as PDT agents. The study findings further establish the potential of Rf–CeO_2 NPs as a multifunctional nanoplatform for targeted breast cancer therapy.

Author contributions

Anongnat Wongpan: conceptualization, methodology, visualization, investigation, formal analysis, writing – original draft, writing – review & editing. Sopon Nuchpun: methodology, visualization, investigation, writing – original draft. Napasorn Tana-atsawapon: methodology, investigation, writing – original draft. Patraporn Luksirikul: supervision, methodology, funding acquisition, writing – review & editing, resources. Sarisa Suriyarak: supervision, methodology, funding acquisition, writing – review & editing. Jintana Artsanthia: supervision, methodology, funding acquisition, writing – review & editing. Kanlaya Prapainop Katewongsa: supervision, conceptualization, methodology, funding acquisition, writing – review & editing, resources, project administration.

Conflicts of interest

There are no conflicts to declare.

Data availability

The data supporting this article have been included as part of the SI.

Supplementary information: dynamic light scattering (DLS) analysis, anti-cancer effect of Rf–CeO_2 with or without UV exposure on MDA-MB-231 cells, cytotoxicity of Rf–CeO_2 with or without UV exposure in normal breast cells (MCF-10A), and relative fluorescence intensity of DCFDA dye analyzed by a microplate reader. See DOI: **https://doi.org/10.1039/d5na00555h**.

Acknowledgements

Authors thank Assoc. Prof. Ekasith Somsook for the use of the instrument. This research project was funded by Mahidol University (Fundamental Fund: Fiscal Year 2024 by the National Science Research and Innovation Fund [NSRF] [FF-079/2567]). Partial support was also provided by a grant from the Center for Scientific Instrumentation and Platform Services, Faculty of Science, Mahidol University. A. W. was supported by a post-doctoral fellowship award from Mahidol University. S. N. was supported by the Development and Promotion of Science and Technology Talents Project. P. L. would like to thank the Kasetsart University Research Development Institute (KURDI) FF(KU)23.67, Kasetsart University and the departments at the Center for Advanced Studies in Nanotechnology for Chemical, Food, and Agricultural Industries, Kasetsart University Institute for Advanced Studies, Kasetsart University.

Notes and references

1 S. Loibl, P. Poortmans, M. Morrow, C. Denkert and G. Curigliano, Breast cancer, *Lancet*, 2021, **397**, 1750–1769, DOI: **10.1016/s0140-6736(20)32381-3**.
2 S.-K. Lee, *et al.*, Nanowire Substrate-Based Laser Scanning Cytometry for Quantitation of Circulating Tumor Cells, *Nano Lett.*, 2012, **12**, 2697–2704, DOI: **10.1021/nl2041707**.
3 B. M. Dicheva, *et al.*, Cationic Thermosensitive Liposomes: A Novel Dual Targeted Heat-Triggered Drug Delivery Approach for Endothelial and Tumor Cells, *Nano Lett.*, 2013, **13**, 2324–2331, DOI: **10.1021/nl3014154**.
4 M. Kanapathipillai, *et al.*, Inhibition of Mammary Tumor Growth Using Lysyl Oxidase-Targeting Nanoparticles to Modify Extracellular Matrix, *Nano Lett.*, 2012, **12**, 3213–3217, DOI: **10.1021/nl301206p**.
5 G. Zhao and B. L. Rodriguez, Molecular targeting of liposomal nanoparticles to tumor microenvironment, *Int. J. Nanomed.*, 2013, **8**, 61–71, DOI: **10.2147/ijn.S37859**.
6 B. E. Hickey and M. Lehman, Partial breast irradiation *versus* whole breast radiotherapy for early breast cancer, *Cochrane Database Syst. Rev.*, 2021, **8**, CD007077, DOI: **10.1002/14651858.CD007077.pub4**.
7 M. S. Wason and J. Zhao, Cerium oxide nanoparticles: potential applications for cancer and other diseases, *Am. J. Transl. Res.*, 2013, **5**, 126–131.
8 J. Saranya, *et al.*, Cerium Oxide/Graphene Oxide Hybrid: Synthesis, Characterization, and Evaluation of Anticancer Activity in a Breast Cancer Cell Line (MCF-7), *Biomedicines*, 2023, **11**, 531.
9 H. Sadidi, *et al.*, Cerium Oxide Nanoparticles (Nanoceria): Hopes in Soft Tissue Engineering, *Molecules*, 2020, **25**, 4559.
10 Y. Lan, *et al.*, Insight into the Contributions of Surface Oxygen Vacancies on the Promoted Photocatalytic Property of Nanoceria, *Nanomaterials*, 2021, **11**, 1168.
11 S. L. Swartz, Catalysis by ceria and related materials, ed. A. Trovarelli, Catalytic Science Series, vol. 2, Imperial College Press, London, 2002, *J. Am. Chem. Soc.*, 2002, **124**, 12923–12924, DOI: **10.1021/ja025256e**.
12 M. Javad Farhangi, A. Es-Haghi, M. E. Taghavizadeh Yazdi, A. Rahdar and F. Baino, MOF-Mediated Synthesis of CuO/CeO(2) Composite Nanoparticles: Characterization and Estimation of the Cellular Toxicity against Breast Cancer Cell Line (MCF-7), *J. Funct. Biomater.*, 2021, **12**, 53, DOI: **10.3390/jfb12040053**.
13 J. Colon, *et al.*, Cerium oxide nanoparticles protect gastrointestinal epithelium from radiation-induced damage by reduction of reactive oxygen species and upregulation of superoxide dismutase 2, *Nanomedicine*, 2010, **6**, 698–705, DOI: **10.1016/j.nano.2010.01.010**.
14 J. L. Y. Tang, S. S. Moonshi and H. T. Ta, Nanoceria: an innovative strategy for cancer treatment, *Cell. Mol. Life Sci.*, 2023, **80**, 46, DOI: **10.1007/s00018-023-04694-y**.
15 X. An, *et al.*, Oxidative cell death in cancer: mechanisms and therapeutic opportunities, *Cell Death Dis.*, 2024, **15**, 556, DOI: **10.1038/s41419-024-06939-5**.

16 H. Choi, *et al.*, Disruption of redox balance in glutaminolytic triple negative breast cancer by inhibition of glutaminase and glutamate export, *Neoplasia*, 2025, **61**, 101136, DOI: 10.1016/j.neo.2025.101136.
17 E. Bibb, *et al.*, Internalized Nanoceria Modify the Radiation-Sensitivity Profile of MDA MB231 Breast Carcinoma Cells, *Biology*, 2021, **10**, 1148, DOI: 10.3390/biology10111148.
18 S. M. Swain, M. Shastry and E. Hamilton, Targeting HER2-positive breast cancer: advances and future directions, *Nat. Rev. Drug Discovery*, 2023, **22**, 101–126, DOI: 10.1038/s41573-022-00579-0.
19 E. Agostinetto, G. Curigliano and M. Piccart, Emerging treatments in HER2-positive advanced breast cancer: keep raising the bar, *Cell Rep. Med.*, 2024, **5**, 101575, DOI: 10.1016/j.xcrm.2024.101575.
20 P. Chen, *et al.*, Higher dietary folate intake reduces the breast cancer risk: a systematic review and meta-analysis, *Br. J. Cancer*, 2014, **110**, 2327–2338, DOI: 10.1038/bjc.2014.155.
21 M. Darguzyte, N. Drude, T. Lammers and F. Kiessling, Riboflavin-Targeted Drug Delivery, *Cancers*, 2020, **12**, 295.
22 A. A. Karande, L. Sridhar, K. S. Gopinath and P. R. Adiga, Riboflavin carrier protein: a serum and tissue marker for breast carcinoma, *Int. J. Cancer*, 2001, **95**, 277–281, DOI: 10.1002/1097-0215(20010920)95:5<277::aid-ijc1047>3.0.co;2-y.
23 K. Thakur, S. K. Tomar, A. K. Singh, S. Mandal and S. Arora, Riboflavin and health: a review of recent human research, *Crit. Rev. Food Sci. Nutr.*, 2017, **57**, 3650–3660, DOI: 10.1080/10408398.2016.1145104.
24 A. B. Witte, *et al.*, Biophysical characterization of a riboflavin-conjugated dendrimer platform for targeted drug delivery, *Biomacromolecules*, 2012, **13**, 507–516, DOI: 10.1021/bm201566g.
25 R. Majumder, *et al.*, Riboflavin-Induced DNA Damage and Anticancer Activity in Breast Cancer Cells under Visible Light: A TD-DFT and *In Vitro* Study, *J. Chem. Inf. Model.*, 2024, **64**, 5580–5589, DOI: 10.1021/acs.jcim.4c01104.
26 J. Yue, *et al.*, Riboflavin-based carbon dots with high singlet oxygen generation for photodynamic therapy, *J. Mater. Chem. B*, 2021, **9**, 7972–7978, DOI: 10.1039/D1TB01291F.
27 W. Mekseriwattana, *et al.*, Riboflavin–citrate conjugate multicore SPIONs with enhanced magnetic responses and cellular uptake in breast cancer cells, *Nanoscale Adv.*, 2022, **4**, 1988–1998, DOI: 10.1039/D2NA00015F.
28 W. Mekseriwattana, T. Thiangtrongjit, O. Reamtong, P. Wongtrakoongate and K. P. Katewongsa, Proteomic Analysis Reveals Distinct Protein Corona Compositions of Citrate- and Riboflavin-Coated SPIONs, *ACS Omega*, 2022, **7**, 37589–37599, DOI: 10.1021/acsomega.2c04440.
29 W. Mekseriwattana, *et al.*, Proteomic Analysis and Molecular Dynamics Simulation of Riboflavin-Coated Superparamagnetic Iron Oxide Nanoparticles Reveal Human Serum-Derived Protein Coronas: Implications as Magnetic Resonance Imaging Contrast Agents, *ACS Appl. Nano Mater.*, 2023, **6**, 13952–13964, DOI: 10.1021/acsanm.3c01767.
30 S. Nuchpun, *et al.*, Uptake Mechanism of Riboflavin-Functionalized Superparamagnetic Iron Oxide Nanoparticles in Triple-Negative Breast Cancer Cells, *ACS Appl. Bio Mater.*, 2025, **8**, 6088–6099, DOI: 10.1021/acsabm.5c00649.
31 W. Mekseriwattana, *et al.*, Dual Functions of Riboflavin-functionalized Poly(lactic-*co*-glycolic acid) Nanoparticles for Enhanced Drug Delivery Efficiency and Photodynamic Therapy in Triple-negative Breast Cancer Cells, *Photochem. Photobiol.*, 2021, **97**, 1548–1557, DOI: 10.1111/php.13464.
32 N. Thakur, *et al.*, Folic acid-functionalized cerium oxide nanoparticles as smart nanocarrier for pH-responsive and targeted delivery of morin in breast cancer therapy, *Inorg. Chem. Commun.*, 2022, **145**, 109976, DOI: 10.1016/j.inoche.2022.109976.
33 A. M. Orville, G. T. Lountos, S. Finnegan, G. Gadda and R. Prabhakar, Crystallographic, spectroscopic, and computational analysis of a flavin C4a-oxygen adduct in choline oxidase, *Biochemistry*, 2009, **48**, 720–728, DOI: 10.1021/bi801918u.
34 M. Culica, C.-S. Andreea, V. Melinte and S. Coseri, Cellulose Acetate Incorporating Organically Functionalized CeO_2 NPs: Efficient Materials for UV Filtering Applications, *Materials*, 2020, **13**, 2955, DOI: 10.3390/ma13132955.
35 E. Kanchana, U. Sampath, C. Yern Chee and H. Noothalapati, Chitosan/Gelatin/Nanocellulose-Based System for Ophthalmic Drug Delivery, *BioNanoScience*, 2024, **15**, 42, DOI: 10.1007/s12668-024-01621-8.
36 Q. Jiao, *et al.*, The latest progress in research on triple negative breast cancer (TNBC): risk factors, possible therapeutic targets and prognostic markers, *J. Thorac. Dis.*, 2014, **6**, 1329–1335.
37 F. Podo, *et al.*, Triple-negative breast cancer: present challenges and new perspectives, *Mol. Oncol.*, 2010, **4**, 209–229, DOI: 10.1016/j.molonc.2010.04.006.
38 P. Vinitha, M. V. Arularasu and R. Vignesh, A review on green synthesis and applications of CeO_2 nanomaterials – an eco-friendly approach, *Chem. Inorganic Mater.*, 2025, **5**, 100084, DOI: 10.1016/j.cinorg.2024.100084.
39 J. Dowding, T. Dosani, A. Kumar, S. Seal and W. Self, Cerium oxide nanoparticles scavenge nitric oxide radical (NO), *Chem. Commun.*, 2012, **48**, 4896–4898, DOI: 10.1039/c2cc30485f.
40 Z. Atlı Şekeroğlu, V. Şekeroğlu, B. Aydın and S. Kontaş Yedier, Cerium oxide nanoparticles exert antitumor effects and enhance paclitaxel toxicity and activity against breast cancer cells, *J. Biomed. Mater. Res., Part B*, 2023, **111**, 579–589, DOI: 10.1002/jbm.b.35175.
41 M. Insińska-Rak, M. Sikorski and A. Wolnicka-Glubisz, Riboflavin and its Derivates as Potential Photosensitizers in the Photodynamic Treatment of Skin Cancers, *Cells*, 2023, **12**, 2304, DOI: 10.3390/cells12182304.
42 S. Criado and N. A. García, Vitamin B2-sensitised photooxidation of the ophthalmic drugs Timolol and Pindolol: kinetics and mechanism, *Redox Rep.*, 2004, **9**, 291–297, DOI: 10.1179/135100004225006047.

43 Z. Frost, S. Bakhit, C. N. Amaefuna, R. V. Powers and K. V. Ramana, Recent Advances on the Role of B Vitamins in Cancer Prevention and Progression, *Int. J. Mol. Sci.*, 2025, **26**, 1967.

44 A. N. Al-Jamal, *et al.*, Photodynamic Therapy (PDT) in drug delivery: nano-innovations enhancing treatment outcomes, *Health Sci. Rev.*, 2025, **14**, 100218, DOI: **10.1016/j.hsr.2025.100218**.

45 F. Sivandzade, A. Bhalerao and L. Cucullo, Analysis of the Mitochondrial Membrane Potential Using the Cationic JC-1 Dye as a Sensitive Fluorescent Probe, *Bio-Protoc.*, 2019, **9**(1), DOI: **10.21769/BioProtoc.3128**.

46 K. Wang, *et al.*, Structure and transport mechanism of human riboflavin transporters, *Nat. Commun.*, 2025, **16**, 4078, DOI: **10.1038/s41467-025-59255-7**.

47 N. Tang, *et al.*, Riboflavin ameliorates mitochondrial dysfunction *via* the AMPK/PGC1α/HO-1 signaling pathway and attenuates carbon tetrachloride-induced liver fibrosis in rats, *Exp. Ther. Med.*, 2022, **24**, 608, DOI: **10.3892/etm.2022.11545**.

48 B. Shanti and Y.-L. Joy, Riboflavin metabolism: role in mitochondrial function, *J. Transl. Genet. Genomics*, 2020, **4**, 285–306, DOI: **10.20517/jtgg.2020.34**.